“Tectonic stress controls saucer-shaped sill geometry”

R.J. Walker and S.P.A Gill

This manuscript has been submitted for publication in *GEOLOGY*. Please note that the manuscript has not undergone peer review. Subsequent versions of this manuscript may have different content. If accepted, the final version of this manuscript will be available via the “peer-reviewed Publication DOI” link on the right-hand side of this webpage.

Please feel free to contact the authors directly to comment on the manuscript. Constructive feedback is welcomed.

Tectonic stress controls saucer-shaped sill geometry.

R.J. Walker[1*] and S.P.A. Gill[2]

[1]University of Leicester, School of Geography, Geology, and the Environment, University Road, Leicester, LE1 7RH, UK.

[2]University of Leicester, Department of Engineering, University Road, Leicester, LE1 7RH, UK.

*Corresponding author: rich.walker@le.ac.uk

ABSTRACT

Saucer-shaped sills are common in sedimentary basins worldwide. The saucer shape relates to asymmetric stress distributions at the sill-tip during intrusion caused by bending of the overburden. Most saucer-shaped sill models are conducted without tectonic stress. Model results are poorly correlated with natural sills in that: (1) modelled saucers are much steeper than natural sills; and (2) natural sill inclines are convex in profile whereas modelled saucer inclines are concave. We present finite element simulation of initially horizontal sill emplacement for a range of tectonic stress (σ_r) conditions, from mild horizontal tension ($\sigma_r < 0$), to horizontal compression ($0 < \sigma_r$). Response to σ_r falls into four regimes, as a ratio of the modelled magma source overpressure (P_o): (I) sills quickly transition to a dike where $\sigma_r/P_o < 0$; (II) steep-climbing extension-mode sills where $0 < \sigma_r/P_o < 1$; (III) gently-climbing extensional-(micro)shear sills where $1 < \sigma_r/P_o < 2$; and (IV) steep-climbing extensional-shear mode sills where $1 < \sigma_r/P_o$. Modelled sills in regime III closely match natural sill geometries. Horizontal compression is critical in controlling the flat base sill length, and the angle of climb from horizontal, by subduing asymmetric stress ahead of the sill tip. Tectonic stress therefore represents a primary control on saucer-shaped sill geometry.

INTRODUCTION

Over the past decade, igneous sills have been increasingly recognized as a major contributor to magma transport through, and storage within, Earth's crust (Leat, 2008; Muirhead et al., 2014). Numerical models for centrally-fed igneous sills emplaced into isotropic elastic media (Malthe-Sorenssen et al., 2004), and analogue models for sill intrusion using homogenous granular media (e.g., Galland et al., 2009), indicate that transgressive saucer-shaped sills are a fundamental geometry in shallow intrusive systems. Such saucer-like geometries are recognized in sedimentary basins worldwide (e.g., Hansen et al., 2004; Cartwright and Hansen, 2006; Thomson, 2007; Hansen, 2011), comprising a relatively flat inner sill that transitions on the periphery to an inward-dipping inclined (transgressive) plane (e.g., Fig. 1A); in several cases, a flat outer-rim is also observed (Malthe-Sorenssen et al., 2004).

Recent studies of inclined sills (Walker et al., 2017; Stephens et al., 2017,2018), and saucer-shaped sills (Walker, 2016) indicate that sill geometry can be strongly controlled by the tectonic stress state at the time of sill emplacement. Most analogue and numerical models for igneous sill emplacement are conducted without tectonic stress. The rationale for this omission is that although it is recognized that sills correspond to a vertical minimum compressive stress ($\sigma_{zz} = \sigma_3$; here we reckon compressive stress positive, where $\sigma_3 \leq \sigma_2 \leq \sigma_1$) (Anderson, 1936, 1951), sills are typically treated as forming by deflection from diking, in response to a local rotation of the stress axes (from

horizontal σ_3, to vertical). Deflection is typically considered to relate to host rock layer heterogeneity (Kavanagh et al., 2006; Gudmundsson, 2011); not a far-field tectonic stress. The deviation from the lithostatic stress (P_L, where σ_3=σ_1) is considered negligible. Analogue models (Galland et al., 2009; Galland and Scheibert, 2013) and numerical simulations for sill growth (Malthe-Sorenssen et al., 2004; Chen et al., 2017), and for static sill-induced fracture (Haug et al., 2017, 2018), under initially lithostatic conditions feature a transition from a flat intrusion to a variably inclined sheet. However, comparison with natural examples of saucer-shaped sills (e.g., Fig. 1) show that the inclined sheet is (a) generally much steeper than natural cases, and (b) the incline profile is concave, compared to the convex profile of natural sills. Modelled inclines in the literature (Fig. 1B) are the result of elastic bending of the overburden (Malthe-Sorenssen et al., 2004), or shear failure of the host material induced by a blunted sill tip (Haug et al., 2017). Elastic bending above the sill results in an asymmetric stress concentration at the sill tip, favouring inclined propagation at some critical ratio (r_c) of flat-sill radius (r) relative to the initial depth (H). Typically, r_c is $1H$ to $2H$ in models, but can be $> 3H$ in nature (Fig. 1B). In contrast, analogue sill experiments in elastic media performed by Bunger et al., (2008) showed that the effect of asymmetric stress distribution ahead of the sill tip can be opposed by applying a horizontal (radial) stress, leading to flatter sills with increasing horizontal stress (Fig. 1B).

Here we use a finite element (FE) simulation to demonstrate the importance of the ambient stress state in controlling saucer-shaped sill geometry during growth, and reconcile the difference between modelled geometries and those in nature. We show that saucer-shaped sill geometry relates to the interplay of the asymmetric stress generated by overburden uplift (promoting steep transgression), and horizontal stress (promoting flattening for small compressive stresses).

METHODS

We implemented an axisymmetric FE model of sill propagation, incorporating coupled processes of linear elastic deformation of the host rock, damage mechanics for rock fracture, and fluid flow for magma movement, in COMSOL Multiphysics (v5.3). The model domain is 8 km deep with radius 16 km, and consists of linear 4-noded square elements with an initial side length (w_0) of 20 m (Fig. 2A,B). Horizontal sills of height 20 m and length 100 m are seeded at a vertical depth (H) of 1 km below the free surface. As is standard in crack band damage models, we apply a linear shape function so that non-physical stresses are not resolved at the square corners of the modelled sill tip (Gill and Walker, in review). The Young's modulus (E_0) of the rock is 1 GPa, with a Poisson's ratio (ν) of 0.4. Magma viscosity (μ) is constant at 10^6 Pa·s and the Bulk Modulus of the magma (K_f) is 0.1 GPa. The rock density (ρ_r) is 2500 kg/m^3 and the magma density (ρ_m) is 2300 kg/m^3. Accounting for the rock density, at depth H the lithostatic stress (here also considered hydrostatic, where $\sigma_1 = \sigma_3$) is approximately 25 MPa (where $P_L = \rho_r g h$, $g = 9.81 m/s^2$ is the acceleration due to gravity, and h is the depth). Two failure criteria for the host rock are implemented: (1) mode I tensile failure, which occurs when $\sigma_3 = \sigma_T = -3MPa$ (the tensile strength of the rock); and (2) Mohr-Coulomb shear failure with shear failure stress $\tau_f = \sigma_n tan\phi + C$, where σ_n is the normal stress on the failure plane, $C = 20MPa$ is the material shear cohesion, and $tan\phi = 30°$ is the angle of internal friction for the host material. Horizontal stress σ_∞ is applied to the external boundary of the model to simulate tectonic stress. We will refer to the differential horizontal stress σ_r ($\sigma_\infty - P_L$): σ_r is zero

when the state of stress is lithostatic, negative in tension ($\sigma_\infty < P_L$), and positive in compression ($P_L < \sigma_\infty$).

The exact criteria for intrusion propagation are not well known as they depend on the local conditions at the propagation front, such as the sharpness of the tip. Sill propagation in the model is achieved by applying a constant magma overpressure $P_o = 5MPa$ at the sill source. P_o is the excess to P_L, and is the reference state for other stress measures in the model. The magma pressure decays along the sill with naturally developing pressure gradients driving magma flow from the source to the tip. Tensile (mode I) failure is determined from the stress required to achieve fracture at the tip: here $\sigma_T^{FE} = -1.2P_o$. This is not a physical parameter, as its value depends on the FE mesh as well as the initial sill geometry. Stresses at a sharper sill tip would be higher than those calculated in a spatially coarser model. The shear failure stress $\tau_f^{FE} = 1.44P_o$ is determined relative to σ_T^{FE}, such that $\tau_f^{FE} = \psi\sigma_T^{FE}$, where $\psi \approx sin\phi + \frac{C}{\rho gH} cos\phi = 1.19$, the ratio of the actual Mohr-Coulomb shear failure stress (τ_f) to the actual tensile failure stress (σ_T) determined at the appropriate depth. The actual material properties are finally related to the FE material properties by determining the apparent fracture toughness of the rock ($K_{Ic}^{FE} = 0.116P_o\sqrt{H}$) in the FE model. This approach considers global energy changes and is not reliant on the accurate determination of localised stresses at the sill tip. Bunger et al., (2008) introduced a dimensionless parameter χ as a means to define scale-independent factors affecting sill profiles (Fig. 1B): $\chi = \sigma_r\sqrt{H}/K_{Ic}$. Inserting the fracture toughness allows the equivalent parameter in the FE model to be expressed as $\chi^{FE} = 8.6\,\sigma_r/P_o$ for comparison. Further details about the model, and the effect of changing ψ is investigated in Gill and Walker (in review).

RESULTS

Figure 2 shows the results of four simulations in which σ_r is 0, 1.2, 5, and 13 MPa, selected from the broader range of simulations: $-1.2MPa \leq \sigma_r \leq 20MPa$. Figure 3 shows the profiles for sills across the range of σ_r tested in this study, normalised to the original depth H (1 km). Note that the steps in the profiles are an artefact of the model mesh. Sill growth behaviour can be divided into four regimes (Fig. 4): (I) horizontal tension ($\sigma_r/P_o < 0$), which results in a rapid transition of the initial sill to a vertical or near-vertical dike (Fig. 3A); (II) a zero to mildly compressive stress ($0 < \sigma_r/P_o < 1$) which results in a decrease in sill incline and increase in sill base length (Fig. 3A); and (III) moderate compressive stress ($1< \sigma_r/P_o < 2$), which causes flat sills; and (IV) large compressive stress ($1 < \sigma_r/P_o$) which causes sill inclines to increase (Fig. 3B). It is noted that the modelled sills show a transition in profile geometry, from concave profiles for $-1.2 < \sigma_r < 0\ MPa$, to convex profiles for $0.3 < \sigma_r < 20\ MPa$. Notably, most analogue models (e.g., Galland et al., 2009) and numerical simulations (e.g., Malthe-Sorenssen et al, 2004; Haug et al., 2017) show concave profiles, but natural sill inclines are convex (e.g. Fig. 1). The effect of σ_r on sill shape, in terms of the critical base length r_c and incline θ, is summarised in Figure 4. Sills in regime I show the shortest base lengths ($< 1.5H$), with r_c reaching its maximum ($\sim 4.5H$) at the regime II-III transition.

DISCUSSION

Horizontal stress has a pronounced effect on intrusion geometry. In regime I ($\sigma_r < 0$) the initially seeded sill quickly transitions to a dike, even at these very low values of applied tension. In regime

II the sill propagates as a mode I extension fracture. The angle of incline is strongly controlled in the models by the angle of maximum energy release rate, which shows only a minor variation (<5°) dependent on the magma pressure profile within the sill (Gill and Walker, *in review*). The incline of the sill relates to bending of the overburden, which induces an out-of-plane tensile stress at the tip preferentially above the sill plane (Malthe-Sorenssen et al, 2004). Stress is additive, and increasing σ_r, even by a small amount, subdues this asymmetry, promoting a flatter sill. At $\sigma_r = 0$, the sill climbs at ~25°, and by σ_r= 5 MPa, this is reduced to ~1° (Fig. 4), at least for the simulated radial distances $< 8H$ (Fig. 3). Normalising sill dimensions to the original depth H allows comparison of the modelled sills with natural examples (Fig. 3; see also Bunger et al., 2008). The results at the lower stress range of regime II (in the range $0 < \chi < 3$) compare favourably with scaled analogue model results of Bunger et al. (2008) (Fig. 4). Sills in regime III, modelled between $5 < \sigma_r < 10\ MPa$ ($8.6 < \chi < 17.2$), show a good fit to the natural saucer-shaped sills shown in Figures 1 and 3; models where $\sigma_r = 0$ show a very poor fit (Fig. 1B and 3). In regime IV, large σ_r results in a shortening of the sill base (r_c) and an increase in sill incline (θ) similar to saucer-shaped sills emplaced during identified phases of horizontal tectonic shortening (e.g., the Stremoy Sill, shown in Figure 1; Walker, 2016).

At distance from the sill, a tectonic stress of σ_r generates a maximum shear stress τ_{max} at of $\frac{1}{2}\sigma_r$ at 45^o to the horizontal. The propagation of the sill through this stressed medium is complex, as it is controlled by the localised stresses generated at the sill tip due to the pressurised magma interacting with σ_r. The larger the value of σ_r, the larger the shear stress τ experienced at the growing sill tip, which increases the likelihood of failure by extensional shear (e.g., Sibson, 1998, 2000; Ramsey and Chester, 2004; Paterson and Wong, 2005). Mohr-Coulomb failure becomes important in regime III of our simulations, and in regime IV the intrusion propagates as a mixed mode I-II extensional shear fracture. Previous studies have highlighted the potential for sills to resolve a component of shear within the plane (Walker, 2016; Walker et al., 2017; Stephens et al., 2017, 2018; Coetzee et al., 2019) as part of an extensional-shear conjugate array, in cases where the tectonic stress is relatively large. Shear across the modelled intrusions here is largely controlled by their incline. The resolved shear stress on the sill plane is $\tau = \frac{\sigma_r}{2}\sin 2\theta$, hence even at very large values for σ_r, a near-horizontal or near-vertical plane experiences very low τ. In our models, τ becomes significant (>2 MPa) on inclined sill planes where $\sigma_r \geq 11MPa$ because this coincides with an increase in sill incline to $\theta > 10°$.

Magnitudes of stress in the simulations are relative to the magma overpressure P_o required to induce failure at the tip. As noted above, the modelled sills are rectangular in section, rather than bladed or elliptical geometries which are common in nature, and in models for dikes (Pollard et al., 1973; Mastin and Pollard, 1988; Rivalta et al., 2015). The rectangular tip requires a greater magnitude of P_o to facilitate propagation, than would be the case for sharp or bladed tips (Vachon and Hieronymus, 2017). Bladed geometries that propagate in mode I result in a maximum stress concentration K that is in plane with the intrusion (Rubin and Pollard, 1988; Maccaferri et al., 2010). Sharp tips also efficiently focus the stress concentration ahead of the tip, leading to failure at low applied stresses. Our modelled tips are blunt, which is less efficient at concentrating stress. Tip bluntness also has the effect of offsetting the maximum stress concentration from in-plane, to the positions of maximum tip curvature, i.e., the corners of a rectangular tip (Poppe et al., 2019); as

noted though, such non-physical stresses are not resolved at the square corners of our modelled sill tips (Gill and Walker, in review). In a dike model, tip blunting could result in different deformation styles above shallow intrusions; extensional grabens above bladed dikes (Mastin and Pollard, 1988), versus fold-and-thrust systems above rectangular tips (Hardy, 2016). In a sill model, tip-blunting can lead to a piston-like effect, in which the intrusion cannot propagate in plane (Haug et a., 2017). In such a case, the sill would grow in thickness rather than radially, causing the overburden to be jacked up vertically, and inducing shear faults at the periphery. Accurately modelling the tip geometry, including as it evolves with changes to the host rock properties and magma viscosity, is an important future target for scaled intrusion modelling.

CONCLUSIONS

Horizontal compressive tectonic stress has a primary control on saucer-shaped sill geometry, reducing the effect of asymmetric tensile stress ahead of the sill tip during growth. Minor compressive stress leads to sill flattening, allowing sills to grow as flat intrusions for long distances, even at shallow levels in the crust, without climbing toward the surface. Larger tectonic stress promotes a transition from extension mode to extensional-shear mode propagation, suggesting that not all sills represent extension fractures. Our models suggest that observed natural saucer-shaped sills are only possible if a horizontal deviatoric tectonic stress is present during their emplacement; sills emplaced during horizontal extension are unstable, and ultimately transition to a dike. This is important for constraining regional stress states, particularly in sedimentary basins and passive margin settings, as sills may provide useful constraint on tectonic stress states during their emplacement.

ACKNOWLEDGEMENTS

REFERENCES

Bunger, A.P., Jeffrey, R.G. and Detournay, E., 2008. Evolution and morphology of saucer-shaped sills in analogue experiments. Geological Society, London, Special Publications, 302(1), pp.109-120.

Cartwright, J. and Møller Hansen, D., 2006. Magma transport through the crust via interconnected sill complexes. Geology, 34(11), pp.929-932.

Chen, T., Cheng, S., Fang, Q. and Zhou, C., 2017. Numerical modeling of shallow magma intrusions with finite element method. Journal of Volcanology and Geothermal Research, 333, pp.53-65.

Coetzee, A., Kisters, A.F.M. and Chevallier, L., 2019. Sill complexes in the Karoo LIP: Emplacement controls and regional implications. Journal of African Earth Sciences, p.103517.

Galland, O. and Scheibert, J., 2013. Analytical model of surface uplift above axisymmetric flat-lying magma intrusions: Implications for sill emplacement and geodesy. Journal of Volcanology and Geothermal Research, 253, pp.114-130.

Galland, O., Planke, S., Neumann, E.R. and Malthe-Sørenssen, A., 2009. Experimental modelling of shallow magma emplacement: Application to saucer-shaped intrusions. Earth and Planetary Science Letters, 277(3-4), pp.373-383.

Gill and Walker, in review. Finite element simulations of sill intrusion during tectonic loading. (*Available via https://eartharxiv.org*).

Gudmundsson, A., 2011. Deflection of dykes into sills at discontinuities and magma-chamber formation. Tectonophysics, 500(1-4), pp.50-64.

Hansen, J. 2011. Petrogenetic Evolution, Geometries and Intrusive Styles of the Early Cenozoic Saucer-Shaped Sills of the Faroe Islands. Doctoral thesis, Durham University.

Hansen, D.M., Cartwright, J.A. and Thomas, D., 2004. 3D seismic analysis of the geometry of igneous sills and sill junction relationships. Geological Society, London, Memoirs, 29(1), pp.199-208.

Haug, Ø.T., Galland, O., Souloumiac, P., Souche, A., Guldstrand, F. and Schmiedel, T., 2017. Inelastic damage as a mechanical precursor for the emplacement of saucer-shaped intrusions. Geology, 45(12), pp.1099-1102

Haug, Ø.T., Galland, O., Souloumiac, P., Souche, A., Guldstrand, F., Schmiedel, T. and Maillot, B., 2018. Shear Versus Tensile Failure Mechanisms Induced by Sill Intrusions: Implications for Emplacement of Conical and Saucer-Shaped Intrusions. Journal of Geophysical Research: Solid Earth, 123(5), pp.3430-3449.

Kavanagh, J.L., Menand, T. and Sparks, R.S.J., 2006. An experimental investigation of sill formation and propagation in layered elastic media. Earth and Planetary Science Letters, 245(3-4), pp.799-813.

Leat, P.T., 2008. On the long-distance transport of Ferrar magmas. Geological Society, London, Special Publications, 302(1), pp.45-61.

Maccaferri, F., Bonafede, M. and Rivalta, E., 2010. A numerical model of dyke propagation in layered elastic media. Geophysical Journal International, 180(3), pp.1107-1123.

Malthe-Sørenssen, A., Planke, S., Svensen, H., Jamtveit, B., Breitkreuz, C. and Petford, N., 2004. Formation of saucer-shaped sills. Physical geology of high-level magmatic systems. Geological Society, London, Special Publications, 234, pp.215-227.

Mastin, L.G. and Pollard, D.D., 1988. Surface deformation and shallow dike intrusion processes at Inyo Craters, Long Valley, California. Journal of Geophysical Research: Solid Earth, 93(B11), pp.13221-13235

Muirhead, J.D., Airoldi, G., White, J.D. and Rowland, J.V., 2014. Cracking the lid: Sill-fed dikes are the likely feeders of flood basalt eruptions. Earth and Planetary Science Letters, 406, pp.187-197.

Paterson, M.S. and Wong, T.F., 2005. Experimental rock deformation-the brittle field. Springer Science & Business Media.

Pollard, D.D., Muller, O.H. and Dockstader, D.R., 1975. The form and growth of fingered sheet intrusions. Geological Society of America Bulletin, 86(3), pp.351-363.

Poppe, S., Holohan, E.P., Galland, O., Buls, N., Van Gompel, G., Keelson, B., Tournigand, P.Y., Brancart, J., Hollis, D., Nila, A. and Kervyn, M., 2019. An Inside Perspective on Magma Intrusion: Quantifying 3D Displacement and Strain in Laboratory Experiments by Dynamic X-Ray Computed Tomography. Frontiers in Earth Science, 7, p.62.

Ramsey, J.M. and Chester, F.M., 2004. Hybrid fracture and the transition from extension fracture to shear fracture. Nature, 428(6978), p.63.

Rivalta, E., Taisne, B., Bunger, A.P. and Katz, R.F., 2015. A review of mechanical models of dike propagation: Schools of thought, results and future directions. Tectonophysics, 638, pp.1-42.

Rubin, A.M. and Pollard, D.D., 1988. Dike-induced faulting in rift zones of Iceland and Afar. Geology, 16(5), pp.413-417.

Sibson, R.H., 1998. Brittle failure mode plots for compressional and extensional tectonic regimes. Journal of Structural Geology, 20(5), pp.655-660.

Sibson, R.H., 2000. Fluid involvement in normal faulting. Journal of Geodynamics, 29(3-5), pp.469-499.

Stephens, T.L., Walker, R.J., Healy, D., Bubeck, A., England, R.W. and McCaffrey, K.J., 2017. Igneous sills record far-field and near-field stress interactions during volcano construction: Isle of Mull, Scotland. Earth and Planetary Science Letters, 478, pp.159-174.

Stephens, T.L., Walker, R.J., Healy, D., Bubeck, A. and England, R.W., 2018. Mechanical models to estimate the paleostress state from igneous intrusions. Solid earth.

Thomson, K., 2007. Determining magma flow in sills, dykes and laccoliths and their implications for sill emplacement mechanisms. Bulletin of Volcanology, 70(2), pp.183-201.

Vachon, R. and Hieronymus, C.F., 2016. Effect of host-rock rheology on dyke shape, thickness and magma overpressure. Geophysical Journal International, 208(3), pp.1414-1429.

Walker, R.J., 2016. Controls on transgressive sill growth. Geology, 44(2), pp.99-102

Walker, R.J., Healy, D., Kawanzaruwa, T.M., Wright, K.A., England, R.W., McCaffrey, K.J.W., Bubeck, A.A., Stephens, T.L., Farrell, N.J.C. and Blenkinsop, T.G., 2017. Igneous sills as a record of horizontal shortening: The San Rafael subvolcanic field, Utah. GSA Bulletin, 129(9-10), pp.1052-1070.

FIGURES

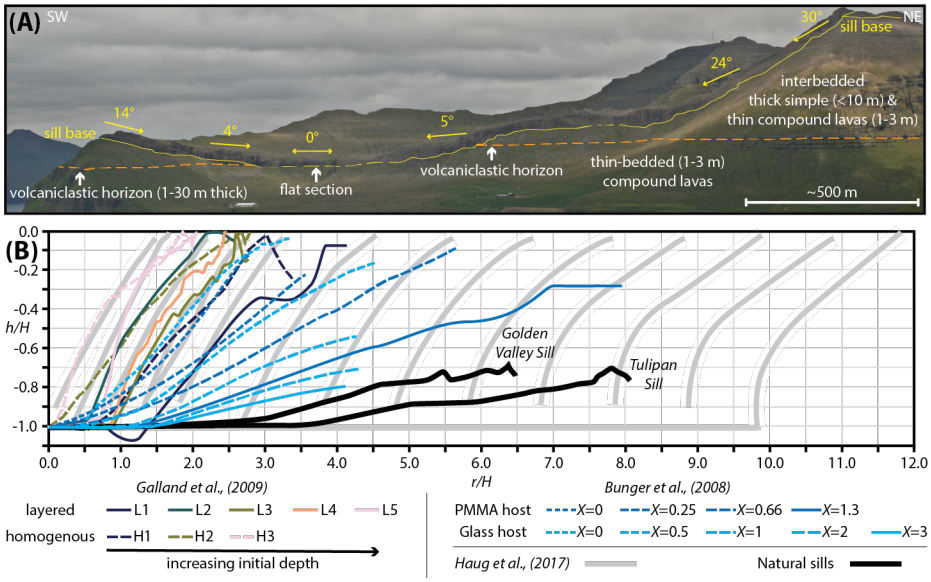

Fig. 1. Saucer-shaped sill geometry in nature and in models from the literature. **(A)** The Streymoy sill, Faroe Islands shows a flat inner region, which transitions to an inward-dipping periphery. Sill dips are taken from Hansen et al., (2011). **(B)** Normalised plots of modelled sill profiles (Bunger et al., 2008; Galland et al., 2009; Haug et al., 2017), and natural sills (Galland et al., 2009). H is the initial depth of intrusion, *h* is the depth, and *r* is the intrusion radius. Galland et al., (2009) used silica powder and vegetable oil for the host rock and magma analogues respectively. Bunger et al., (2008)

used glass or PMMA, and water. They also introduced a dimensionless parameter χ, where $\chi = \sigma_r\sqrt{H}/K_{Ic}$. K_{Ic} is 1.3 and 0.6 MPa m$^{1/2}$ for their PMMA and glass respectively. Haug et al., (2017) used a rigid-plasticity approach to simulate sills in a homogenous Mohr-Coulomb material. The 'sills' in their models did not grow in length; individual plots show the damage associated with cracks of variable starting length. Starting depth H was 2 km, and sill thickness was 50 m.

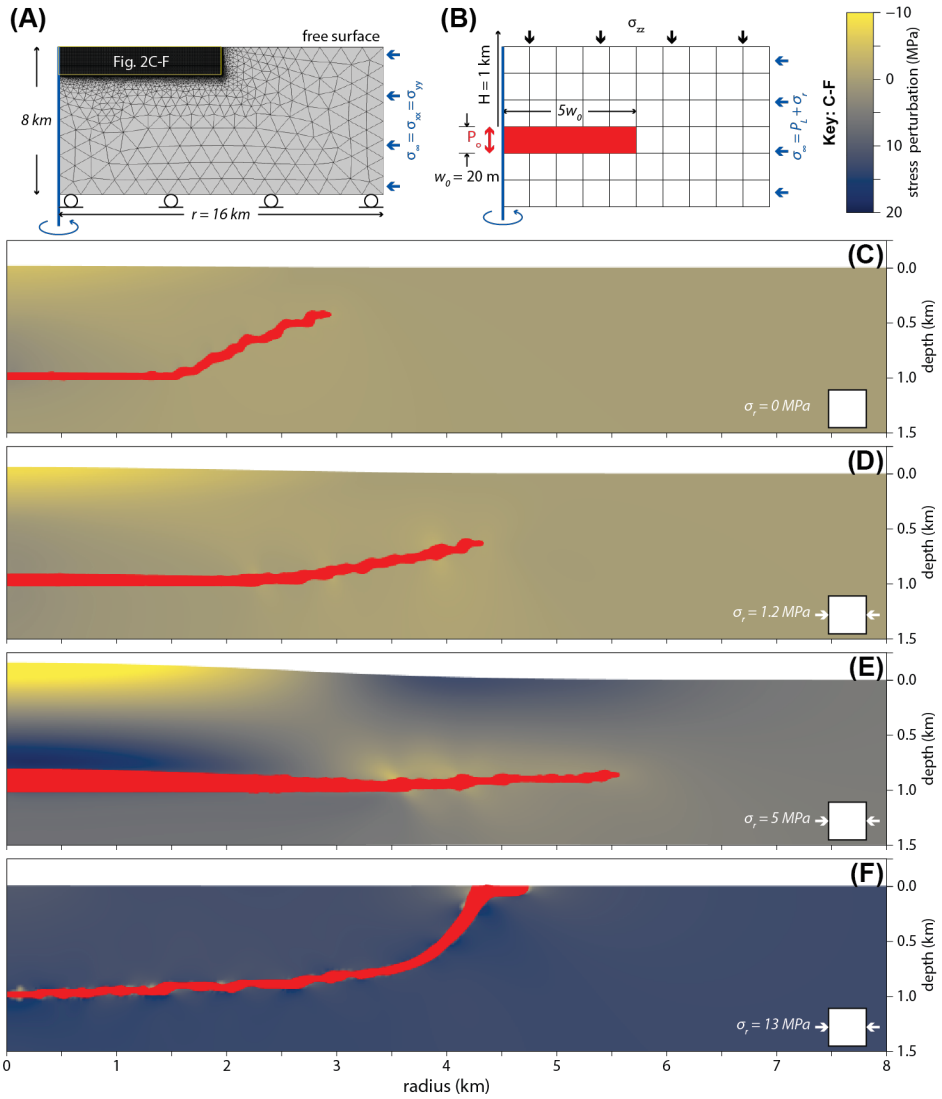

Fig. 2. Model set-up and examples of intrusion simulation results showing the role of σ_r in controlling intrusion geometry. **(A)** Model domain consists of an unstructured mesh to move boundaries far from the sills, with **(B)** a square-noded grid in the region of the sills. Models are axisymmetric about the blue line. **(C-F)** Simulation results for σ_r at 0, 1.2, 5, and 13 MPa. Note that only the stress perturbation is shown (i.e. stress minus P_L).

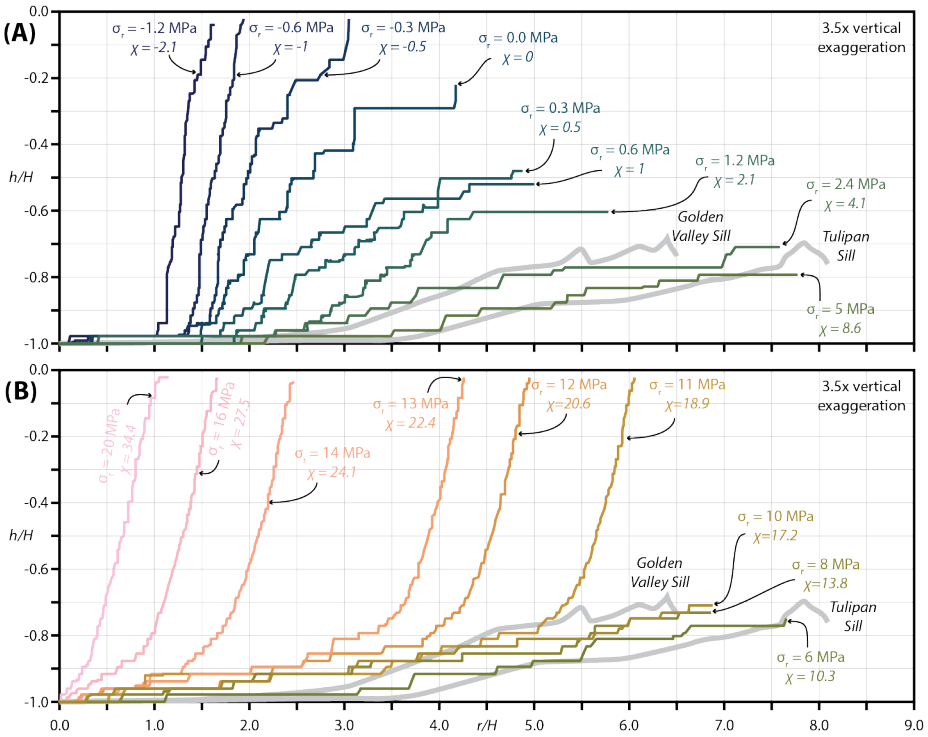

Fig. 3. Normalised intrusion profiles as a function of σ_r. **(A)** Tensile to mildly-compressive σ_r. **(B)** Strongly-compressive σ_r. See Figure 1 for details of χ.

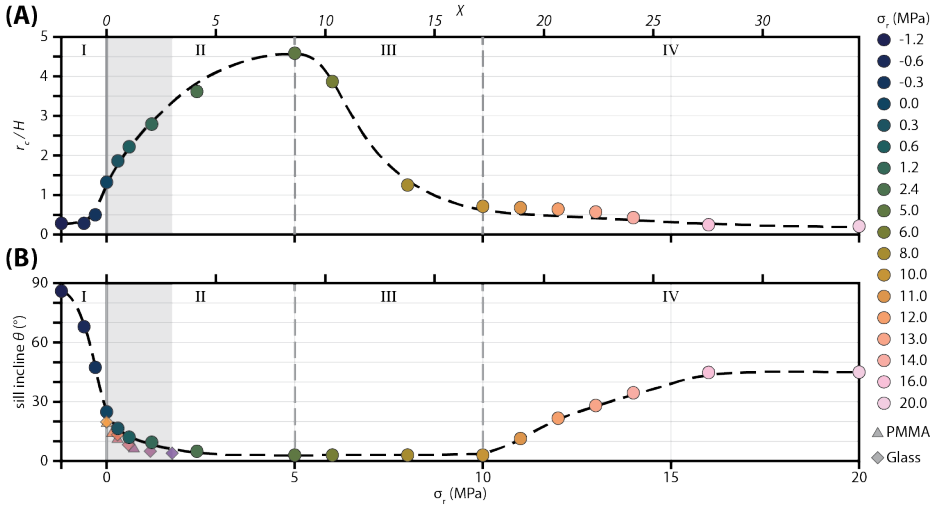

Fig. 4. Summary of results for **(A)** sill base length and **(B)** sill incline angle θ for the studied range of σ_r. Grey regions show the range of χ values for the scaled analogue models of Bunger et al., (2008); results from their PMMA and glass experiments are also shown.